



Originally published as:

Orlecka-Sikora, B., Cesca, S., Lasocki, S., Lizurek, G., Wiejacz, P., Rudzinski, L. (2014): Seismogenesis of exceptional ground motion due to a sequence of mining induced tremors from Legnica-Gogow Copper District in Poland. - *Geophysical Journal International*, 198, 1, p. 40-54

DOI: <http://doi.org/10.1093/gji/ggu109>

Seismogenesis of exceptional ground motion due to a sequence of mining induced tremors from Legnica-Głogów Copper District in Poland

Beata Orlecka-Sikora,¹ Simone Cesca,² Stanisław Lasocki,¹ Grzegorz Lizurek,¹ Paweł Wiejacz¹ and Łukasz Rudziński¹

¹*Institute of Geophysics, Polish Academy of Sciences, Warsaw, Poland. E-mail: orlecka@igf.edu.pl*

²*GeoForschungsZentrum Potsdam, Potsdam, Germany*

Accepted 2014 March 20. Received 2014 March 15; in original form 2012 November 29

SUMMARY

A series of six seismic events that occurred in one panel of Rudna copper-ore mine in Poland is studied. Although the events had comparable magnitudes, from 3.0 to 3.7, their ground effects were very diverse. Comparing the accelerations observed at various locations with their estimates from ground motion prediction equation the events split into three distinct pairs. The first pair ground effects exceed considerably the estimates at most of observation points, the second pair effects are abnormally high at short epicentral distances, whereas the third pair effects are much less than the estimates at most of observation points. The similarities in ground effects correlate with the fault mechanisms similarities. The first two pairs' events, whose ground effects were strong, exhibit thrust faulting and the third pair events, which caused unexpectedly low ground motion exhibit normal faulting mechanisms. The paired events have also similar apparent stress values. These stress values of the two events of very weak ground effects are distinctly lower than the values of other four events. All events demonstrate dominating non-double-couple components in the overall mechanisms. A kinematic source analysis indicates that these events have extended rather than point sources, and five of them have distinct directivity effects. A static stress transfer analysis signifies interrelations between these events. The rupture of all events started in areas of Coulomb failure function increase due to the cumulative effect of previous events. Linking results of the ground effects, source, rupture and interaction analyses tentative geodynamic conclusions are formulated. The untypical and diverse ground effects of the studied events result likely from the events' complexity expressed by tensile source mechanisms, finite sources, directivity of ruptures and nearly horizontal rupture planes. The above features seem to be implied by a superposition of coseismic alterations of stress field and stress changes due to mining. One cannot, therefore, exclude the possibility of other cases of significant deviations from the expected ground motion amplitudes, due to specific geodynamics in another parts of the mine. An analysis like that done within this work can allow, however, foreseeing such extreme surface impacts.

Key words: Earthquake ground motions; Earthquake source observations; Earthquake interaction, forecasting and prediction.

1 INTRODUCTION

Copper-ore excavation in the Legnica-Głogów Copper District (LGCD) in southwest Poland is carried out in three underground mines: Rudna, Polkowice-Sierszowice and Lubin. The ore is extracted from hard rigid rocks at considerable depths, from 800 to 1100 m below the surface. Due to this, mining is accompanied by intense induced seismic activity. The in-mine seismic systems,

installed in each of the three mines, record altogether thousands events annually. The local magnitude of these events ranges from 0.4 to 4.5.

The LGCD is an urbanized area and mining-induced seismic events often affect significantly buildings and surface structures. Among such structures, the Żelazny Most tailings pond, located within a range of mining seismic events impact, requires particular attention. With its area of about 12.4 km² enclosed within 14 km

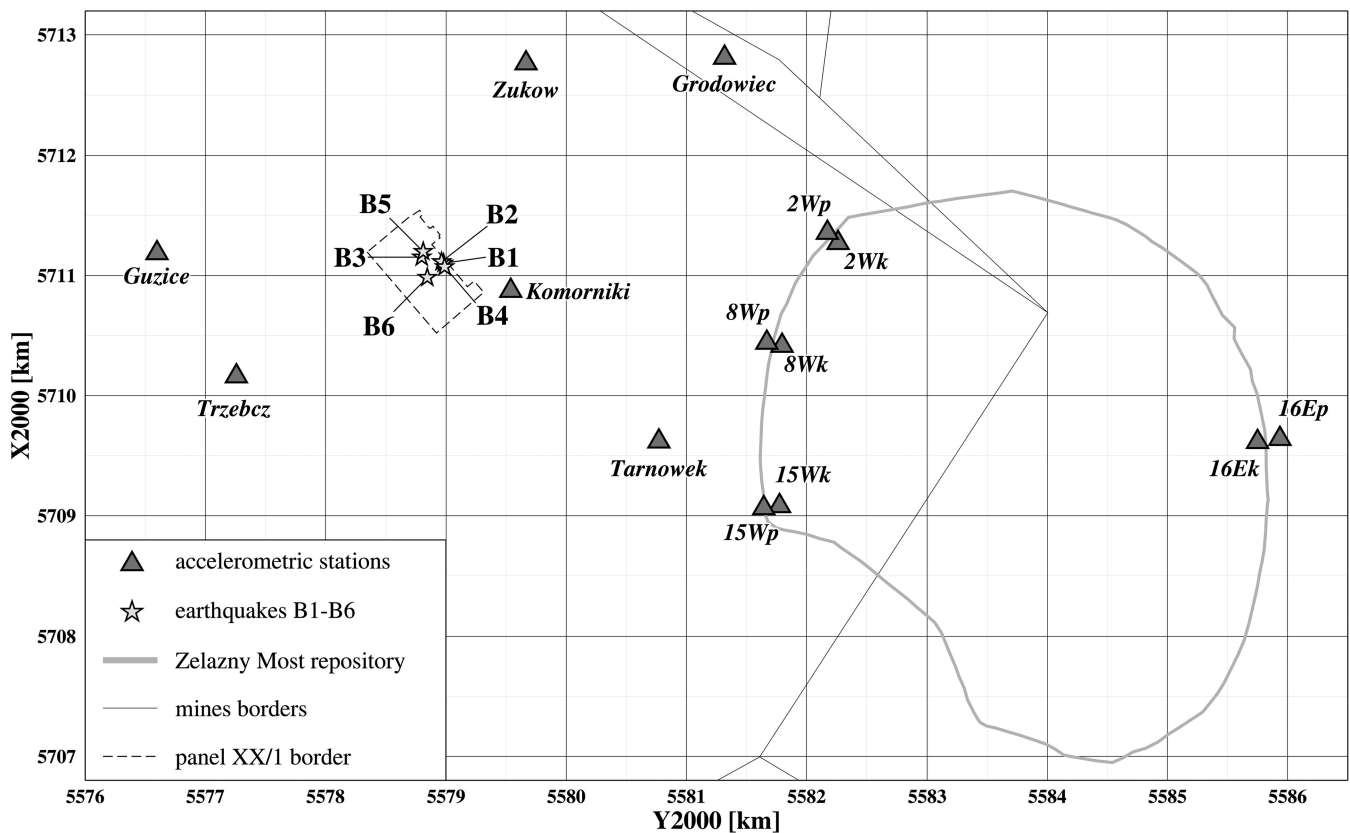


Figure 1. Żelazny Most tailings pond, ground motion monitoring stations and epicentres of the studied tremors from the mining panel XX/1. ‘p’ means the station locations at the base and ‘k’ on the crest of a tailings pond dam.

long by up to 50 m high earth dams and 1 billion m³ of final capacity, the repository is one of the largest waste dumps in the world. In order to ensure its safety the company responsible for the repository has started in 2002 a special program of ground motion monitoring at the repository dams and in the repository’s western foreland. Presently the area is monitored with eight three-component free-field accelerometric stations at the dams and next six on the foreland. Brüel & Kjær sensors are used with a linear response from 0.5 to 100 Hz. Fig. 1 presents locations of these stations. The stations at the dams are coupled, one placed at the base and the other one on the crest of the dam.

Until now more than 2700 three-component ground motion signals has been collected. This data was used, among others, to work out local ground motion prediction equations (GMPE-s) for peak horizontal (PHA) and vertical (PVA) acceleration of motion in the frequency band up to 10 Hz. The frequency content limitation was meant to remove those frequency components, which were unimportant from an engineering standpoint, but which were significant in ground motion caused by relatively weak mining-sources. With increasing bulk of the data the GMPE-s are updated. The most recent GMPE-s that also take into account relative site amplification factors are presented in Lasocki (2013).

Starting from some midst of 2010 untypical seismic events have been occurring in connection with mining works in the panel XX/1 of Rudna mine. The events are of comparable energies and are not exceptionally strong; their magnitude ranges from 3.0 to 3.7. However, ground effects of some of them are strong and extensive, whereas those of others are quite weak. In the present work we study properties of six such events in an attempt to explain reasons of their untypical effects. It turns out that sources of these tremors were

extended with significant non-shearing components. This complexity of sources together with specific rupture directions caused likely the diverse ground effects.

2 SITE AND DATA DESCRIPTION

A productive level of Rudna copper-ore mine is located at the depth from 900 to 1200 m and is overlain and underlain by thick, hard and rigid rock strata. The depth of the ore body, the ability to accumulate strain energy by surrounding rocks and highly variable tectonic conditions constitute grounds for generating violent seismicity and rockbursting. The mine operates an in-mine seismic system, consisting of 32 uniaxial-vertical seismometers. The distance between sensors ranges from 0.5 to 11 km. The system records all events from magnitude 1.2. Event epicentres are determined with the location error less than 50 m, however the seismic network is nearly flat and the hypocentral depth is poorly constrained.

The productive level of panel XX/1 of Rudna mine is located at the depth of about 1100 m and is overlain by some 60–92-m-thick dolomite layer followed upwards by rigid anhydrite strata of around 160 m thickness. Below the deposit is a layer of hard Rotliegendes sandstones of about 300 m thickness. Ore is extracted by means of a room-and-pillar exploitation system. In this system, the ore-seam is cut into passages and chambers separated by structural pillars. In the course of removal of rock the pillars degrade enabling gradual roof subsidence. Productive blasting is carried on in the panel every day at fixed hours. Destressing blasting is done once a week at the last working shift.

Mining works in the panel XX/1 began in 2009 and have been continued until present. From the beginning the exploitation is

Table 1. Occurrence time, source location and magnitude of the studied six strong seismic events from panel XX/1. Focal coordinates are in a local Cartesian system, M_w is the moment magnitude.

Event ID	Occurrence time		Location (m)			Magnitude
	Date	Time	X	Y	Z	M_w
B1	2010 June 26	04:47	5711101	5578981	930	3.5
B2	2010 November 13	05:49	5711112	5578965	975	3.3
B3	2010 December 18	18:03	5711151	5578798	827	3.4
B4	2011 January 20	05:59	5711071	5578987	897	3.1
B5	2011 January 20	06:00	5711197	5578811	827	3.5
B6	2011 June 08	11:39	5710981	5578844	941	3.5

Table 2. Source parameters of six strong seismic events from panel XX/1. The assumed P -wave velocity is $V_P = 5700 \text{ m s}^{-1}$, density of rock mass is $\rho = 2900 \text{ kg m}^{-3}$, radiation coefficient for P wave is 0.52, free surface effect factor = 1, the mean distance seismic source–station are given in the chapter ‘Site description’.

Event ID	Occurrence time		Average spectral level of P waves	Average corner frequency of P waves	Seismic moment	Total seismic energy	Apparent stress
	Date	Time	Ω (m s)	F (Hz)	M_0 (N·m)	E (J)	σ_a (kPa)
B1	2010 June 26	04:47	3.4×10^{-6}	2.8	1.8×10^{14}	1.9×10^8	28.5
B2	2010 November 13	05:49	1.5×10^{-7}	2.6	9.2×10^{13}	8.0×10^7	23.5
B3	2010 December 18	18:03	3.2×10^{-6}	2.0	1.6×10^{14}	1.0×10^8	16.9
B4	2011 January 20	05:59	9.3×10^{-7}	3.5	5.5×10^{13}	4.9×10^7	24.1
B5	2011 January 20	06:00	3.3×10^{-6}	2.2	1.8×10^{14}	2.3×10^8	34.5
B6	2011 June 08	11:39	3.3×10^{-6}	2.7	2.1×10^{14}	4.1×10^8	52.7

accompanied by seismic activity but only from some mid of 2010 stronger tremors have been occurring. A mining seismic catalogue contains 289 events of local magnitude from 1.2 from the period from 2009 May 10 to 2011 July 13. Six of them, stronger, of magnitude 3.1 and more, are investigated in the present study. Four events (B1, B3, B5, B6 in Table 1) took place during excavation works and were considered as a natural rockmass relaxation. The other two events (B2, B4), which occurred just after distressing blasting were most likely triggered by the blasting.

Initial locations of the analysed events, provided by the mine, are corrected using Single Event Relocation Method. In case of the analysed events this relocation method gave more satisfactory results than ‘double-difference relocation method’ (Rudziński & Dębski 2011). The all six events are not clustered when take into account waveforms similarities. It can be noticed that some similarities appear just in pairs, because of that we decided to locate absolute times and positions rather than relative location by double-difference relocation method. Spectral analysis is applied to estimate the scalar seismic moment, seismic energy and apparent stress. The analysis is performed using records of the seismic system of Rudna mine, using the formalism of Andrews (1986), Brune (1970, 1971) and Wyss & Brune (1968), described by Gibowicz & Kijko (1994) and Niewiadomski (1997). The results are provided in Tables 1 and 2. Locations of event epicentres are presented in Fig. 1.

3 GROUND EFFECTS

Ground motion due to all the six tremors was recorded by most of the accelerometric stations monitoring the area of Żelazny Most tailings pond; the missing data cases was due to incidental breakdowns of some stations. The peak horizontal amplitudes (PHA) of ground motion resulting from these tremors are compared with the PHA estimates from the mentioned in the Introduction, local ground motion prediction equation (GMPE). The GMPE takes the form of

(Lasocki 2013):

$$\log PHA_i(m_E, r) = 0.950 + 0.293m_E - 1.192 \log \sqrt{r^2 + 255025} + w_i, \quad i = 1, \dots, 14, \quad (1)$$

where $PHA_i(m_E, r)$ is the peak horizontal acceleration expected at i th station location, $m_E = \log E$ and E is the source seismic energy, r is the source–receiver epicentral distance, w_i is the logarithmized amplification factor at i th station location, relative to a reference station location.

The relative amplification factors are presented in Table 3. Further details on this GMPE are reported in the background publication (Lasocki 2013).

Fig. 2 presents the observed PHA values, the values estimated from (1) and 95 per cent confidence intervals for prediction. *A posteriori* probabilities that the observed PHA-s are not attained

Table 3. Relative amplification factors of GMPE in eq. (1). #10 8W_p is the reference station.

Station	Relative amplification w_i
#1 Zukow	0.0160
#2 Guzice	−0.0083
#3 Trzebcz	0.0781
#4 Tarnowek	0.1199
#5 Grodowiec	0.0774
#6 Komorniki	0.0411
#7 2W _K	−0.0255
#8 2W _P	−0.0057
#9 8W _K	−0.0212
#10 8W _P	0.0000
#11 15W _K	0.0378
#12 15W _P	0.0605
#13 16E _K	0.0830
#14 16E _P	0.0703

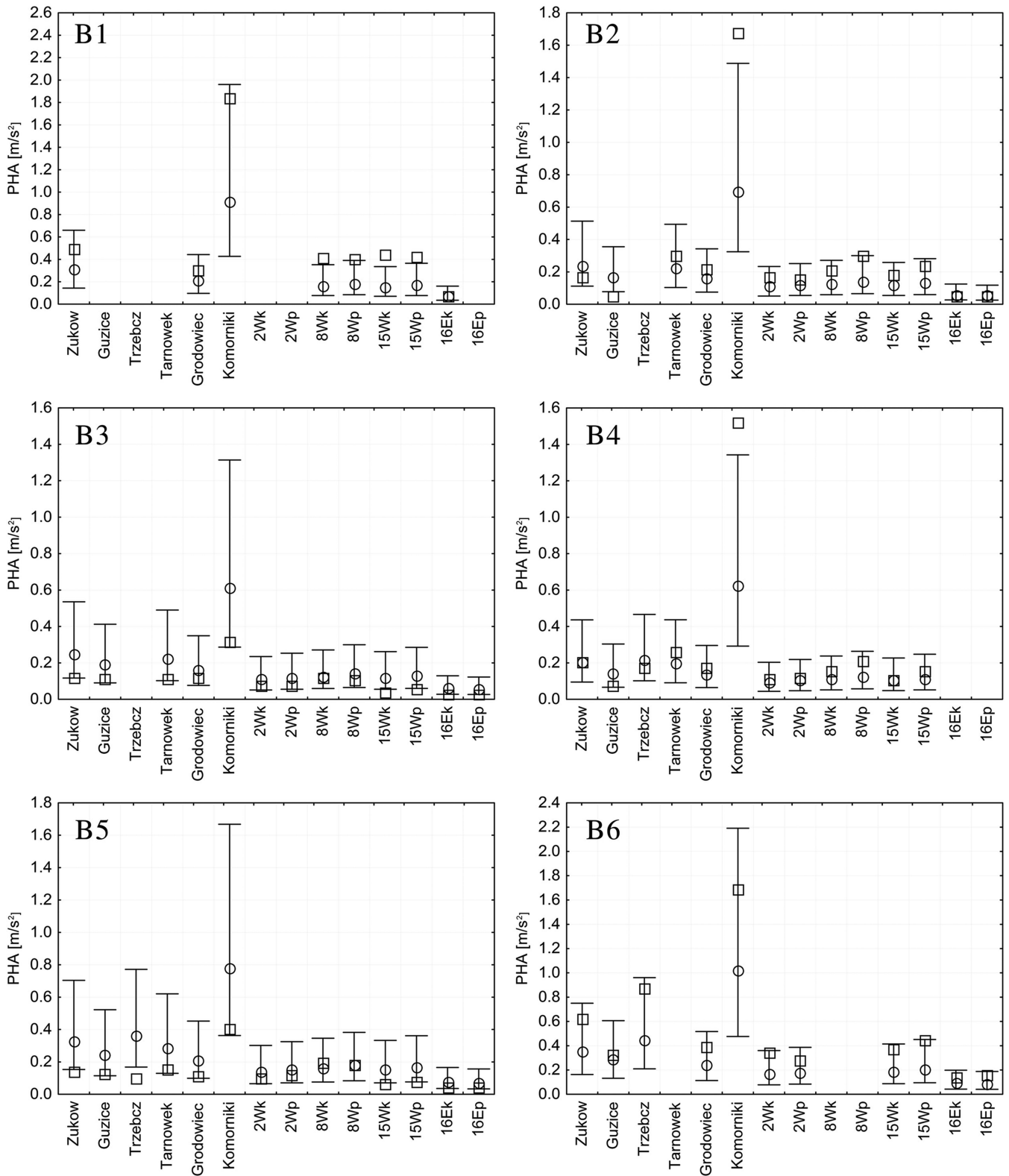


Figure 2. Observed PHA values of ground motion caused by six seismic events from the panel XX/1 with respect to 95 per cent confidence intervals for prediction of the local GMPE (eq. 1). Circles, median estimates. Vertical bars, confidence intervals. Squares, observed values. Locations of measurement points are provided in Fig. 1.

according to GMPE are shown in Fig. 3. It can be seen that in four cases, namely B1, B2, B4 and B6, the actual PHA-s on most of the stations are greater (B2, B4) and fairly greater (B1, B6) than the respective estimated medians, whereas the actual values

much lower than the estimates for other two events (B3, B5). The extreme discrepancies are not linked to the same stations, hence they cannot be attributed to stronger local amplification at certain sites or to preferential propagation conditions along some wave

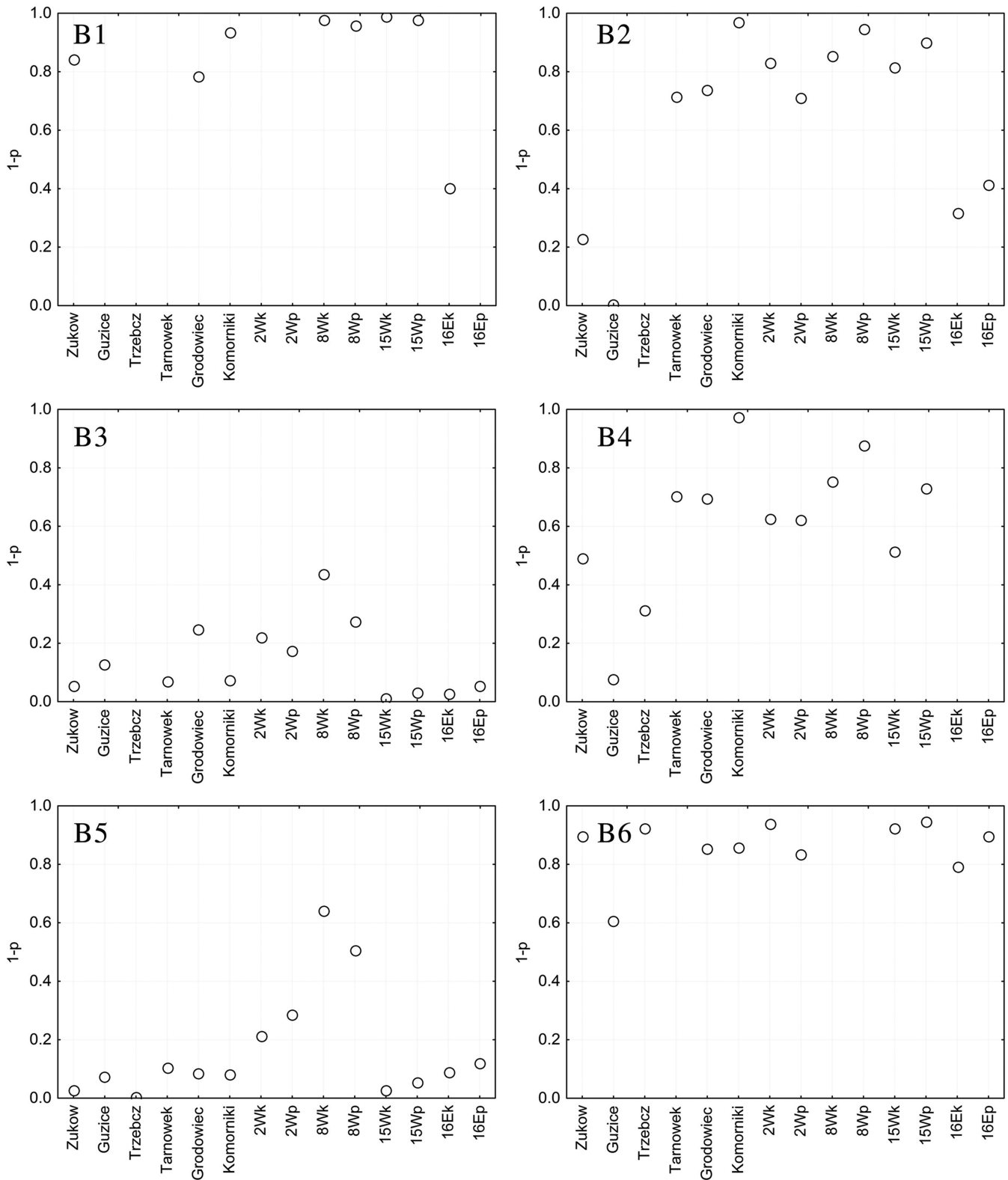


Figure 3. *A posteriori* probability that the observed PHA values of ground motion caused by six seismic events from the panel XX/1 are not attained. The estimation have been done by means of the local GMPE (eq. 1). Locations of measurement points are provided in Fig. 1.

paths. Furthermore, relative local amplification factors are included in the used GMPE (eq. 1). Therefore it is right to concluded that the observed deviations from GMPE estimates result from sources properties.

Based on distinct similarities of pictures in Fig. 2 and of those in Fig. 3 the studied tremors, regarding their ground effects, are split into three groups. The first group comprise B1 and B6. Their actual ground effects on many stations is unusually high. In five out of

eight records due to B1 the probability to attain the PHA values such as the observed is, according to GMPE (eq. 1), less probable than 10 per cent; in six out of eight it is less than 20 per cent. For the B6 case these number are 5 from 11 less probable than 10 per cent and 9 from 11 less probable than 20 per cent. There was only one observation with PHA less than the estimated median in the case of B1, and none such observations in the case of B6.

The effects of the second group of tremors, namely B2 and B4, less deviate from the predicted median values, with the exception for the nearest station Komorniki (620 and 590 m from the source, respectively). It was very improbable to attain the observed PHA at Komorniki due to these two tremors, only 2.9 and 2.7 per cent, respectively. Most of the actual PHA values are above their respective medians but there are some opposite cases: 4 in 13 for B2 and 3 in 12 for B4.

The third group are tremors B3 and B5, whose actual PHA values are mostly below or extremely below the respective estimates. In 7 out of 13 records due to B3 and in 8 out of 14 records due to B5 the occurrence of their PHA values was less probable than 10 per cent; in 9 out of 13 and 10 out of 14 it was less than 20 per cent. The values observed at station 15W_k for event B3 and at station Trzebcz for event B5 were highly improbable, being 1 and 0.22 per cent, respectively.

4 FOCAL MECHANISMS

Focal mechanisms are assessed based on seismic data acquired from an in-mine seismic system. The system consists of 32 short period vertical seismometers. The seismometers are located at the level of copper ore deposit at depth around 1000 m below the surface. Fig. 4 depicts the study area, along with the locations of the in-mine seismic stations and the spatial distribution of the analysed seismic events.

Focal mechanisms are calculated using the moment tensor inversion in time domain (Wiejacz 1992). The calculations are performed with the use of FOCI software (Kwiatk 2011) adjusted to the geological situation within the mine. The input parameters are the first

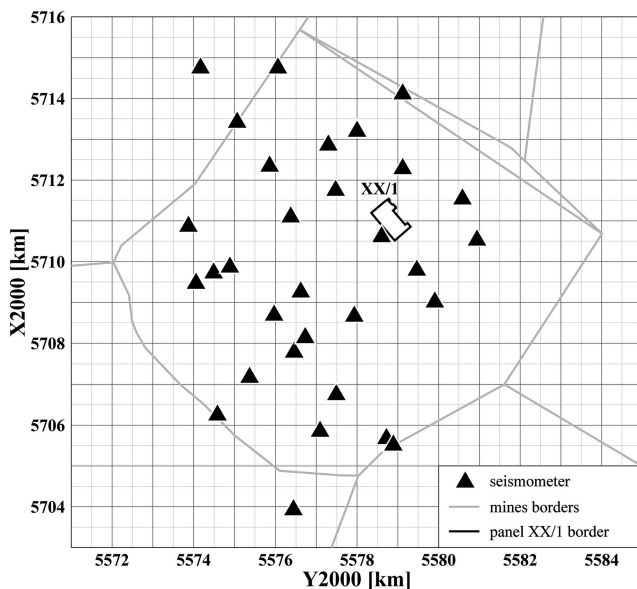


Figure 4. The map of the in-mine network (triangles) used to calculate moment tensor of analysed seismic events. XX/1 mining panel as well as Rudna's mine borders are sketched.

amplitudes and polarities of P waves. In LGCD area at distances <1000 m refracted waves dominate over direct waves in the first P -wave arrivals. We observe head waves refracted from both the crystalline basement composed of igneous rocks, located beneath the exploitation level (incidence angle $\sim 60^\circ$) and anhydrite layer located above this level (incidence angle $\sim 115^\circ$). Both types of waves are used to improve the focal sphere coverage. The velocities determined for the waves are: direct wave is 5 km s^{-1} , the wave refracted above the ore seam is 5.9 km s^{-1} and the wave refracted beneath the seam is 5.6 km s^{-1} (Wiejacz 1992). Haskell's source model is assumed (Haskell 1953), which requires calculating the rupture time from the average first P -wave pulse durations. According to Wiejacz (1991), this model of seismic source is a good approximation of real mining-induced seismic sources in LGCD. All, the full moment tensor, the deviatoric and the pure shear solutions are calculated using the L2 norm and the method of Lagrange multipliers (Wiejacz 1991). Uncertainties are assessed with the use of jackknife method applied to station recordings. The resultant errors are: 20° for strike, 5° for dip and 10° for rake. The mechanisms and their parameters are presented in Table 4. Table presents two types of source mechanisms for each event: the full mechanism and the double couple (DC) mechanism along with the maximum error of the moment tensor components. The error was obtained from covariance matrix of the L2 norm inversion (Wiejacz 1992).

The focal mechanisms are pairwise similar and the tremor pairs are the same as those indicated by the similarity of ground effects. The mechanisms of events from different pairs are distinctly different. The events from two pairs: (B1, B6) and (B3, B5) represent thrust faulting in the full mechanism and the DC mechanism, and events (B2, B4) exhibit normal faulting in the DC mechanism. However, in all six cases non-DC components dominate in the overall mechanisms. The non-shearing components content varies from 56 per cent (event B5) to 85 per cent (event B2). The other common feature of all considered events is a small dip angle of the fault planes, being less than 30° for events B1, B6, less than 10° for events B2 and B4 and a bit more than 30° for events B3 and B5.

5 MODELLING OF SURFACE ACCELERATIONS

Following the moment tensor source models obtained from the waveforms from the underground in-mine seismic system, maximal accelerations recorded by the surface accelerometric network at the Zelazny Most tailings pond are used to infer further information about the source rupture processes. The hypocentral locations are similar for all six events, and cannot explain alone the different patterns of polarities and amplitudes. The observed patterns of accelerations might be therefore linked to different radiation patterns. Waveforms are generally long lasting, which cannot be reproduced assuming simple impulsive source time functions and the chosen 1-D layered velocity model. The observation of simple body-wave pulses at the closest stations and at the in-mine stations seems to indicate that the observed long lasting signals are consequences of propagation effects rather than long lasting source time functions. Because of this features we prefer to limit our inversion and base it on the most stable observations: polarities and maximal amplitudes.

We first consider the similarity of the six events, based on the following observations: (i) PHA values corrected for local effects (Lasocki & Olszewska 2003; Olszewska 2006; Golik & Mendecki 2012; Lasocki 2013), (ii) first motion polarities at accelerometers located at the surface and (iii) first motion polarities at seismic

Table 4. Focal mechanisms of the analysed seismic events from panel XX/1: the full solution (left) and the double couple solution (right). The beachball diagrams are shown in lower hemisphere projections with polarities denoted with '+' and '-' signs. EMT is maximum moment tensor error obtained from covariance matrix in L2 norm inversion.

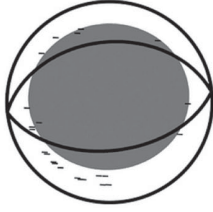

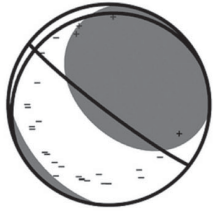
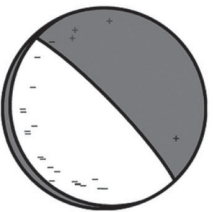
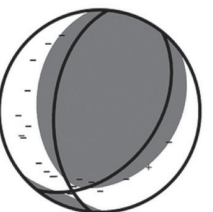
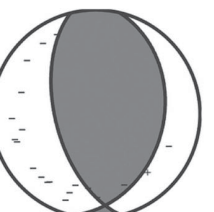
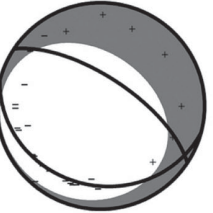
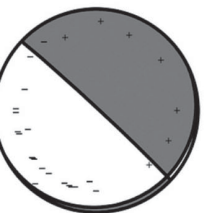
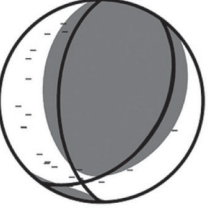
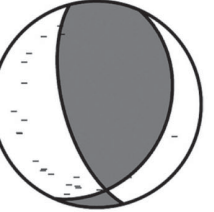
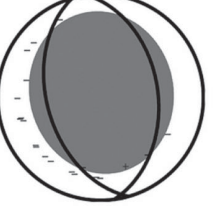
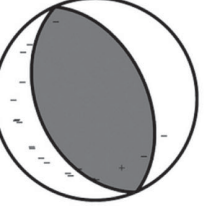
Full mechanism		Double couple mechanism	
<p>B1</p> 	<p>Moment Tensor [N·m]: $M_{11}=-2.82 \cdot 10^{13}$ $M_{22}=-1.83 \cdot 10^{13}$ $M_{12}=9.64 \cdot 10^{11}$ $M_{23}=-1.90 \cdot 10^{12}$ $M_{13}=1.15 \cdot 10^{13}$ $M_{33}=1.03 \cdot 10^{14}$ EMT=$4.2 \cdot 10^{12}$</p> <p>EXPL: 28.0%; CLVD: 55.3%; DC: 16.7%</p> <p>Source mechanism (Strike/Dip/Slip): A: $83.8^\circ/50.1^\circ/89.6^\circ$; B: $264.5^\circ/39.9^\circ/90.5^\circ$</p>		<p>Moment Tensor [N·m]: $M_{11}=1.08 \cdot 10^{13}$ $M_{22}=1.88 \cdot 10^{10}$ $M_{12}=8.78 \cdot 10^{11}$ $M_{23}=-1.69 \cdot 10^{12}$ $M_{13}=6.59 \cdot 10^{12}$ $M_{33}=1.08 \cdot 10^{13}$ EMT=$4.5 \cdot 10^{12}$</p> <p>Source mechanism (Strike/Dip/Slip): A: $80.2^\circ/61.1^\circ/84.9^\circ$; B: $270.6^\circ/29.3^\circ/99.1^\circ$</p>
	<p>Moment Tensor [N·m]: $M_{11}=-1.38 \cdot 10^{12}$ $M_{22}=1.49 \cdot 10^{12}$ $M_{12}=9.02 \cdot 10^{12}$ $M_{23}=1.79 \cdot 10^{13}$ $M_{13}=1.71 \cdot 10^{13}$ $M_{33}=1.68 \cdot 10^{13}$ EMT=$1.6 \cdot 10^{12}$</p> <p>EXPL: 24.0%; CLVD: 61.5%; DC: 14.6%</p> <p>Source mechanism (Strike/Dip/Slip): A: $127.1^\circ/84.7^\circ/80.4^\circ$; B: $245.6^\circ/10.9^\circ/151.0^\circ$</p>		<p>Moment Tensor [N·m]: $M_{11}=1.50 \cdot 10^{12}$ $M_{22}=3.68 \cdot 10^{12}$ $M_{12}=2.55 \cdot 10^{12}$ $M_{23}=1.28 \cdot 10^{13}$ $M_{13}=1.26 \cdot 10^{13}$ $M_{33}=-5.18 \cdot 10^{12}$ EMT=$1.5 \cdot 10^{12}$</p> <p>Source mechanism (Strike/Dip/Slip): A: $316.1^\circ/82.0^\circ/93.1^\circ$; B: $157.1^\circ/8.6^\circ/69.1^\circ$</p>
	<p>Moment Tensor [N·m]: $M_{11}=4.63 \cdot 10^{12}$ $M_{22}=-4.71 \cdot 10^{13}$ $M_{12}=2.98 \cdot 10^{13}$ $M_{23}=4.33 \cdot 10^{13}$ $M_{13}=5.09 \cdot 10^{13}$ $M_{33}=1.94 \cdot 10^{14}$ EMT=$5.1 \cdot 10^{12}$</p> <p>EXPL: 30.9%; CLVD: 32.3%; DC: 36.8%</p> <p>Source mechanism (Strike/Dip/Slip): A: $184.7^\circ/52.5^\circ/67.6^\circ$; B: $38.8^\circ/42.8^\circ/116.4^\circ$</p>		<p>Moment Tensor [N·m]: $M_{11}=1.46 \cdot 10^{12}$ $M_{22}=-2.53 \cdot 10^{13}$ $M_{12}=4.84 \cdot 10^{11}$ $M_{23}=1.05 \cdot 10^{13}$ $M_{13}=6.64 \cdot 10^{12}$ $M_{33}=2.39 \cdot 10^{13}$ EMT=$5.8 \cdot 10^{12}$</p> <p>Source mechanism (Strike/Dip/Slip): A: $165.5^\circ/58.2^\circ/75.0^\circ$; B: $12.5^\circ/34.8^\circ/112.7^\circ$</p>
	<p>Moment Tensor [N·m]: $M_{11}=4.68 \cdot 10^{12}$ $M_{22}=1.55 \cdot 10^{12}$ $M_{12}=8.77 \cdot 10^{11}$ $M_{23}=1.07 \cdot 10^{13}$ $M_{13}=1.07 \cdot 10^{13}$ $M_{33}=-2.72 \cdot 10^{13}$ EMT=$2.2 \cdot 10^{12}$</p> <p>EXPL: -30.4%; CLVD: -46.0%; DC: 23.7%</p> <p>Source mechanism (Strike/Dip/Slip): A: $303.7^\circ/67.1^\circ/82.4^\circ$; B: $104.8^\circ/24.1^\circ/107.4^\circ$</p>		<p>Moment Tensor [N·m]: $M_{11}=2.25 \cdot 10^{12}$ $M_{22}=-9.72 \cdot 10^{11}$ $M_{12}=5.02 \cdot 10^{11}$ $M_{23}=1.20 \cdot 10^{13}$ $M_{13}=1.30 \cdot 10^{13}$ $M_{33}=-1.28 \cdot 10^{12}$ EMT=$2.2 \cdot 10^{12}$</p> <p>Source mechanism (Strike/Dip/Slip): A: $312.5^\circ/87.9^\circ/85^\circ$; B: $64.8^\circ/5.5^\circ/157.6^\circ$</p>
	<p>Moment Tensor [N·m]: $M_{11}=3.79 \cdot 10^{12}$ $M_{22}=-3.87 \cdot 10^{13}$ $M_{12}=2.01 \cdot 10^{13}$ $M_{23}=3.47 \cdot 10^{13}$ $M_{13}=3.36 \cdot 10^{13}$ $M_{33}=1.20 \cdot 10^{14}$ EMT=$5.6 \cdot 10^{12}$</p> <p>EXPL: 26.6%; CLVD: 29.4%; DC: 43.9%</p> <p>Source mechanism (Strike/Dip/Slip): A: $180.0^\circ/55.7^\circ/67.6^\circ$; B: $36.2^\circ/40.2^\circ/119.2^\circ$</p>		<p>Moment Tensor [N·m]: $M_{11}=3.22 \cdot 10^{12}$ $M_{22}=-2.66 \cdot 10^{13}$ $M_{12}=2.23 \cdot 10^{12}$ $M_{23}=1.65 \cdot 10^{13}$ $M_{13}=9.31 \cdot 10^{12}$ $M_{33}=2.34 \cdot 10^{13}$ EMT=$5.9 \cdot 10^{12}$</p> <p>Source mechanism (Strike/Dip/Slip): A: $164.7^\circ/64.1^\circ/70.4^\circ$; B: $23.8^\circ/32.1^\circ/124.6^\circ$</p>
	<p>Moment Tensor [N·m]: $M_{11}=-9.67 \cdot 10^{12}$ $M_{22}=-2.08 \cdot 10^{13}$ $M_{12}=2.27 \cdot 10^{12}$ $M_{23}=1.40 \cdot 10^{12}$ $M_{13}=5.62 \cdot 10^{12}$ $M_{33}=6.00 \cdot 10^{13}$ EMT=$2.0 \cdot 10^{12}$</p> <p>EXPL: 24%; CLVD: 47.5%; DC: 28.5%</p> <p>Source mechanism (Strike/Dip/Slip): A: $164.0^\circ/46.9^\circ/84.1^\circ$; B: $352.5^\circ/43.4^\circ/96.2^\circ$</p>		<p>Moment Tensor [N·m]: $M_{11}=-3.04 \cdot 10^{12}$ $M_{22}=-1.57 \cdot 10^{13}$ $M_{12}=-6.91 \cdot 10^{12}$ $M_{23}=-1.54 \cdot 10^{12}$ $M_{13}=-8.56 \cdot 10^{11}$ $M_{33}=1.87 \cdot 10^{13}$ EMT=$2.0 \cdot 10^{12}$</p> <p>Source mechanism (Strike/Dip/Slip): A: $335.7^\circ/47.7^\circ/89.3^\circ$; B: $156.7^\circ/42.3^\circ/90.7^\circ$</p>

Table 5. Velocity model used for the computation of synthetic accelerograms.

Depth (m)	V_P (km s ⁻¹)	V_S (km s ⁻¹)	Density (g cm ⁻³)
<735	2.90	1.68	2.00
735–835	5.90	3.41	2.85
835–910	4.45	2.57	2.45
910–1310	4.8	2.77	2.30
1310–5000	6.00	3.46	3.00

sensors within the mine. Results confirm the existence of the three couples of similar events. In particular, (i) as addressed in Section 3, based on the patterns of maximal accelerations, couples B1–B6, B2–B4 and B3–B5 can be identified, (ii) based on polarities within the mine, couples B3–B5, B1–B6 are identified.

As the first attempt, maximal recorded horizontal accelerations at the surface are modelled using point source representations, both assuming the preferred DC and full moment tensor (MT) models provided by the moment tensor inversion. Synthetic accelerograms are computed for frequencies below 10 Hz at the surface network using the Kiwi tools (Cesca *et al.* 2010; Heimann 2011), and a layered velocity model (Table 5). Waveform modelling for mining induced seismicity using the Kiwi tools were successfully performed by Cesca *et al.* (2013) and Sen *et al.* (2013). The accelerograms are computed for each event and for both possible (DC and MT) point source models, and the maximal PHA are extracted. Observed and modelled PHA are then scaled to estimate the preferred scalar moment, and finally PHA misfit estimations (using L2 norm) is computed. Observations from station Komorniki increase greatly the misfit and therefore they are excluded from the following modelling and inversion. This station is located at very short epicentral distances and the effects observed there can be influenced by near or intermediate field terms and contain significant non-elastic components. Results indicate that synthetic accelerations for MT models can, in general, fit recorded PHA better than those for respective DC models (Table 6, first two columns).

As the second approach, we consider extended source models to judge whether observed acceleration patterns can be better reproduced by finite sources, when specific rupture geometries and directivity effects are considered. We model finite sources using a distribution of point sources along a circular planar area. Based on the fact that the moment tensor inversion has indicated the domination of the non-DC components for all studied earthquakes, we use full MT solutions as models of these point sources. However, the MT source models have been derived on the base of observed polarities at in-mine stations. In consequence, they reproduce the radiation pattern at the time and location of the rupture nucleation, but cannot be used to infer the geometry of the following rupture process. Whereas in typical tectonic frameworks pure DC sources are found, and the two possible fault plane orientations can be safely used to constrain further investigated finite source models (e.g. see

Cesca *et al.* 2010), the current results question which is the real fault plane orientation. One possibility is to consider the orientation of the non-DC term, often dominant the MT solution and choose a rupture plane oriented perpendicular to the main axis of the compensated linear vector dipole (CLVD). Such a model would correspond to a dominating tensile crack. However, other orientations are possible, for example, those associated to the orientation of the DC component. Vavryčuk (2001, 2011) proposed source models with tensile cracks with opening axis non-perpendicular to the crack plane. A similar model was proposed by Eyre *et al.* (2013) for long period seismic sources in volcanic environments. Let's consider the event couple B1–B6, which reasonably should have a similar source type, as effects in terms of polarity, amplitudes and accelerations are comparable; the inverted full MT solutions are similar, but the DC components very different. We could then argue that either the common MT orientation or any of the two DC models provide some information on the rupture plane orientation. Given the limitations of the available data we do not perform a complete inversion, but rather test a number of possible finite source models and consider those, which are able to reproduce the patterns of maximal accelerations. In our tests we consider only a limited number of source geometries. Our approach is to consider all these possible source geometries discussed before (i.e. perpendicular to the major CLVD axis, or according to the two possible fault planes for the event and its pairwise event) and test all of them in terms of finite sources. Finite sources are composed of several equally distributed point sources, each of them with the given original MT solution, which are excited at different times, in order to reproduce effects of rupture propagation. For each event, we test 750 circular fault models, accounting for different rupture sizes, centroid depths, rupture geometries (as discussed before) and direction of rupture propagations. Five sizes are tested for each event, with radii in a realistic range of 0.5–1.5 times the reference estimations, which are based on spectral analysis at the nearest broadband station of Polish Seismological Network in Książ (www.igf.edu.pl). Five different centroid depths are tested, perturbing the depth estimates in the range ± 50 m, with the step of 25 m.

Finally, for all discussed geometries, five possible rupture directions are considered: in one case the rupture nucleates at the centre of the rupture area (outwards) and in the other four cases at one edge and propagating mostly in a given direction (strikewards, counter strikewards, upwards, downwards). The rupture velocity is fixed for all models to 2.2 km s⁻¹, which is about 0.9 times the *S*-wave velocity at the given range of hypocentral depths. Extended source models are discretized (see Cesca *et al.* 2010; Heimann 2011) into a number of point sources distributed along the chosen geometry and with a common point source model according to the above given strategies. For each finite source model accelerograms and PHA are estimated, scalar moment inverted and L2-norm misfits are used to infer, which rupture model can better fit the data.

Results are summarized in Tables 6 and 7. Results in Table 6 indicate for all events that acceleration patterns fit significantly better when assuming finite ruptures, rather than point sources. The fit improvement is significant, if compared to differences observed assuming DC or full MT sources, suggesting that the acceleration pattern is more link to finite source parameters, such as size or directivity, than to the radiation pattern of the single point source. This finding is also supported by the fact that similar improvements for finite source models are also found, if finite source models of equivalent geometry are built by spatial distribution of different focal mechanisms (e.g. based on the best DC models). Table 7 summarizes the most important source parameters for the preferred

Table 6. Goodness of fit of synthetic to observed PHA-s. For each event, L2 norm misfits are shown for the best point (Pt) and finite (Kin) source models.

Event	Misfit Pt DC	Misfit Pt MT	Misfit Kin MT
B1	0.244	0.136	0.049
B2	0.125	0.102	0.081
B3	0.191	0.168	0.109
B4	0.094	0.079	0.065
B5	0.169	0.150	0.136
B6	0.205	0.241	0.171

Table 7. Final rupture models. h is the source depth. The next four columns provide information on the fault planes with parameters as explained Fig. 5. r is the circular fault radius.

Event	h (m)	Strike Dip		Mechanism (°)			Source size (m)
		Strike	Dip	Rake	Slip azimuth	Slope	r
B1	905	272	29	99	354	57	258
B2	800	157	9	-69	53	60	226
B3	777	24	32	125	79	35	206
B4	872	65	6	-158	38	-48	288
B5	877	13	35	113	80	30	251
B6	891	272	29	99	353	46	240

finite source models: the orientation of the rupture plane in terms of strike, dip and rake angles, the rupture size and the centroid depth. In five out of six events the analysis suggests unidirectional ruptures. An exception is for the event B4 when no specific rupture propagation direction can be distinguished. The rupture of this event is considered to begin in the centre of the fault plane and propagate uniformly in all directions. All preferred ruptures occur along subhorizontal faults, and all events pairs show consistent size and directivity estimations. Preferred source sizes (radii ranging 240–310 m for the six events) are always much larger than the starting values (160–210 m), but lower than estimations based on the spectral analysis of records of each event from the stations in-mine system (340–560 m).

Events B1–B6 have similar MT solutions, whereas DC solutions differs a lot, striking E–W for B1, and SE–NW for B6 (Table 4). Out of four considered extended source geometries the kinematic modelling prefers for both events that one linked to DC solution obtained for B1. For events B1–B6 the ruptures propagate towards S. Preferred models for events B2–B4 indicate ruptures along almost horizontal planes. In the case of B4 event, no directivity effects are detected, indicating that the rupture could propagate from the centre outwards. For events B3–B5 the ruptures propagate toward WNW.

6 STATIC STRESS TRANSFER

The interoccurrence time of the analysed tremors is relatively short and all these events were located close to each other. This suggests that the tremors could be mutually correlated. A seismic event rupture deforms the surrounding rock environment and changes stress field permanently, which in turn can trigger or retard other earthquakes in the region (e.g. Stein 1999; Papadimitriou & Sykes 2001; Hainzl *et al.* 2009; Orlecka-Sikora 2010; Orlecka-Sikora *et al.* 2011). Coseismic static stress changes are generally calculated from dislocation models of the seismic source, expressed in terms of the Coulomb failure function (CFF ; e.g. King *et al.* 1994; King & Cocco 2001) defined as $\Delta CFF = \Delta\tau + \mu'\Delta\sigma$. Here τ is the shear stress on the receiving fault in the slip direction, σ is the normal stress on the receiving fault, positive for extension and μ' is the apparent friction coefficient (Cocco & Rice 2002). A positive changes of CFF ($\Delta CFF > 0$) increase the likelihood of receiving fault rupture, whereas the negative ΔCFF decrease this likelihood.

In order to investigate the influence of Coulomb stress changes caused by the predecessors on the subsequent events within the studied six tremors from the panel XX/1, the Coulomb stress changes due to all previous events are resolved on the rupture plane of the next event in the series. Orlecka-Sikora *et al.* (2012) have shown that although mining activity time variations cause perturbations of stress field around the mine excavations in a short term, Coulomb

stress changes due to coseismic slip can influence the subsequent seismicity within several months. Thus the cumulative static stress changes due to preceding events are considered. Those rupture planes, which are located in increased CFF areas, were brought closer to failure by previous events.

All calculations are performed with the use of Coulomb 3.0 software (Lin & Stein 2004; Toda *et al.* 2005). Based on the results of kinematic analysis (Section 5), extended sources for five tremors, B1, B2, B3, B5 and B6 are assumed. Since the kinematic analysis indicates a multidirectional rupture for the tremor B4, it is modelled here as a point source. Geometrical parameters of sources are those resulted from the kinematic modelling. The applied software requires the assumption of extended source as rectangle. The length of rupture plane scales in proportion to width up to the dimension of seismogenic zone. The seismogenic zone in the panel XX/1 has thickness of around 160 m. Taking into consideration dip of planes and estimated circular fault radius the proportion of planes sides should be around 3:2. Thus the circular fault radii are recalculated into the length and width of the corresponding rectangular faults in this proportion. It is worth noting that we performed specific tests and verify that predicted accelerations are similar for circular rupture model of different sizes, in an attempt to assess the validity the approximation of the circular fault to its equivalent rectangular one (a rectangular model cannot be currently implemented); a variation in the source depth or the rupture directivity produce, in comparison, much larger effects. The coseismic displacement along the ruptured plane is estimated from the seismic moment tensor of the tensile source for isotropic media (Aki & Richards 2002):

$$M_{ij} = uS [\lambda v_k n_k \delta_{ij} + \mu (v_i n_j + v_j n_i)], \quad (2)$$

where u is the mean slip, S is the fault area, λ and μ are the Lamé's constants, n_i , $i = 1, 2, 3$, are the components of normal to the fault plane, v_i are the dislocation directions and δ_{ij} is the Kronecker's delta. For the tensile source n and v are expressed in terms of angles of strike, dip, rake and slope (Vavryčuk 2011; explanation on Fig. 5). Slope, α , characterizes the tensility of the source and is directly evaluated from eigenvalues of moment tensor M_{ij} . The positive slope value is connected with the crack openness, the negative slope value denotes crack closure (Vavryčuk 2001).

Both Lamé's constants are set to 2.7×10^4 MPa, the Poisson ratio value is 0.25 and the apparent coefficient of friction is 0.8. Information on the rupture models and slip of the studied events is given in Tables 7 and 8.

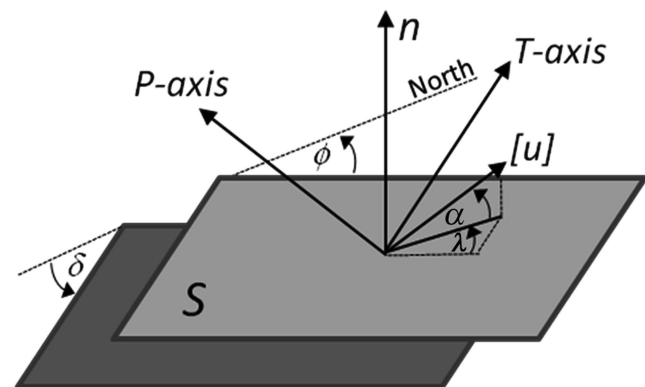


Figure 5. The geometry of a tensile fault earthquake. S is the fault plane area, $[u]$ is the dislocation vector, n is the fault normal and angles ϕ , δ , λ and α are strike, dip, rake and slope (inclination slip).

Table 8. Slip values used in the Coulomb stress transfer calculations. st, ss and sd are the tensile displacement, the displacement along strike direction and the displacement along dip direction, respectively. The slip values calculated assuming the Knopoff and Randall moment tensor decomposition (1970).

Event	Slip (cm)		
	st	ss	sd
B1	2.2	0.2	1.5
B2	1.2	-0.2	-0.6
B3	4.2	3.5	5.0
B4	-0.5	0.4	-0.2
B5	1.6	1.1	2.6
B6	1.2	0.2	1.2

The calculated cumulative Coulomb failure function changes due to previous events on the fault planes of subsequent events are shown in Figs 6–10. In all cases ruptures began either in areas of enhanced stress or at their edges where ΔCFF gradient is high. The B2 rupture started at the place where CFF increased due to event B1 (Fig. 6). Similarly, the rupture of B3 began in the area of stress increase due to cumulative effect of B1 and B2 (Fig. 7). The cross-section along the mining front (Fig. 7b) shows that in the place where B3 event occurred, the Coulomb failure function changes were high.

B1, B2 and B3 events caused the stress changes on the plane of B4 event as presented in Fig. 8. Most of the area being mined after B3 event occurrence experienced negative stress changes. Positive stress changes appeared in the northeast part of the mining front, in the right flank of panel XX/1 and on the boundary of this area and area with negative stress changes B4 occurred. The next event, B5, occurred also in the boundary between the zones of positive and negative stress changes at the end of right flank of the panel (Fig. 9).

An interesting case is that of event B6. Its epicentre is in an unmined part about 200 m ahead of the mining front. Such a location is unusual since in Rudna mine the vast majority of induced events occurring in front of mining works locates not further than 100 m from the works (Kozłowska 2013). Nevertheless, the present location of B6 has been carefully checked and confirmed. The stress transfer analysis results, shown in Fig. 10, indicate that events B1–B5 caused negative stress changes on the plane of event B6 in the most part of the area mined after B5 occurrence. A lobe of $\Delta CFF > 0$ only touches the northeastern part of mining front. When shifting B6 hypocentre downwards of 30 m, which is well in the range of depth estimation uncertainty, the stress enhanced zone narrows further away from the mining front towards the unmined area and B6 event (Fig. 10b). It seems therefore, that the static stress transfer had in this case the decisive influence of the location of B6. The cross-section in Fig. 10(c) shows that the hypocentre of B6 event was located on the boundary between the positive and negative ΔCFF .

7 TENTATIVE GEODYNAMIC CONCLUSIONS

B1 event is nearly a pure thrust fault dipping north of 29.3° , in agreement with the rock strata inclination direction. The epicentre located on the left of the mined out right flank of panel XX/1 (Fig. 11). The rupture began at the depth of 905 m at the contact zone of the dolomite and anhydrite layers some 200 m above the ore-seam. Fracturing propagated upwards towards south, opposite to slip, which was less than 10° from N. It is therefore probable that the foot wall of anhydrite subsided towards the goaf. The appearance of wings, which increased non-DC component, could also be possible (Fig. 12). Such a movement can explain also 57° slope of this event mechanism.

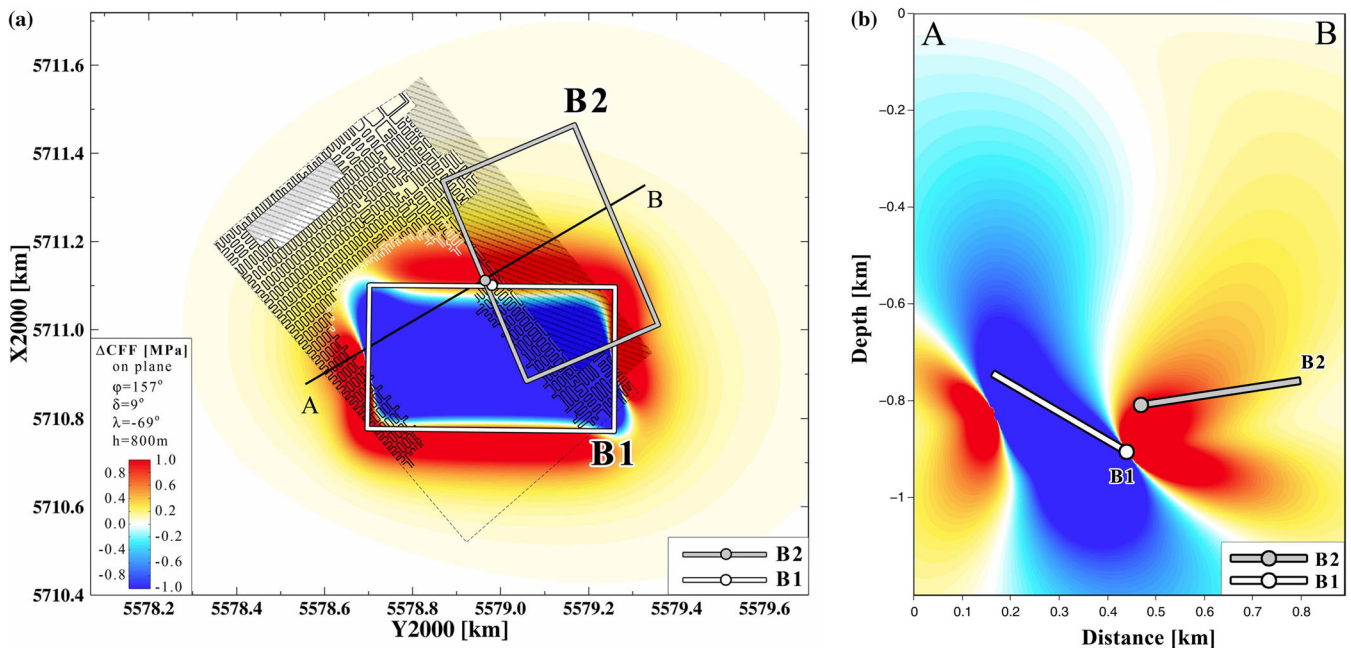


Figure 6. Coulomb stress changes due to event B1 calculated on the fault plane of event B2. (a) Horizontal projection. (b) Vertical cross-section along AB profile from (a). The white dot and white solid lines mark, respectively, the rupture starting point and the fault plane boundary of B1 event and grey dot and grey solid lines mark these objects of B2 event. The cross-hatched area is goaf, the small black rectangles mark a mined-out part and the small white rectangles mark a part being mined from 2010 January 10 to the time of B2 event occurrence.

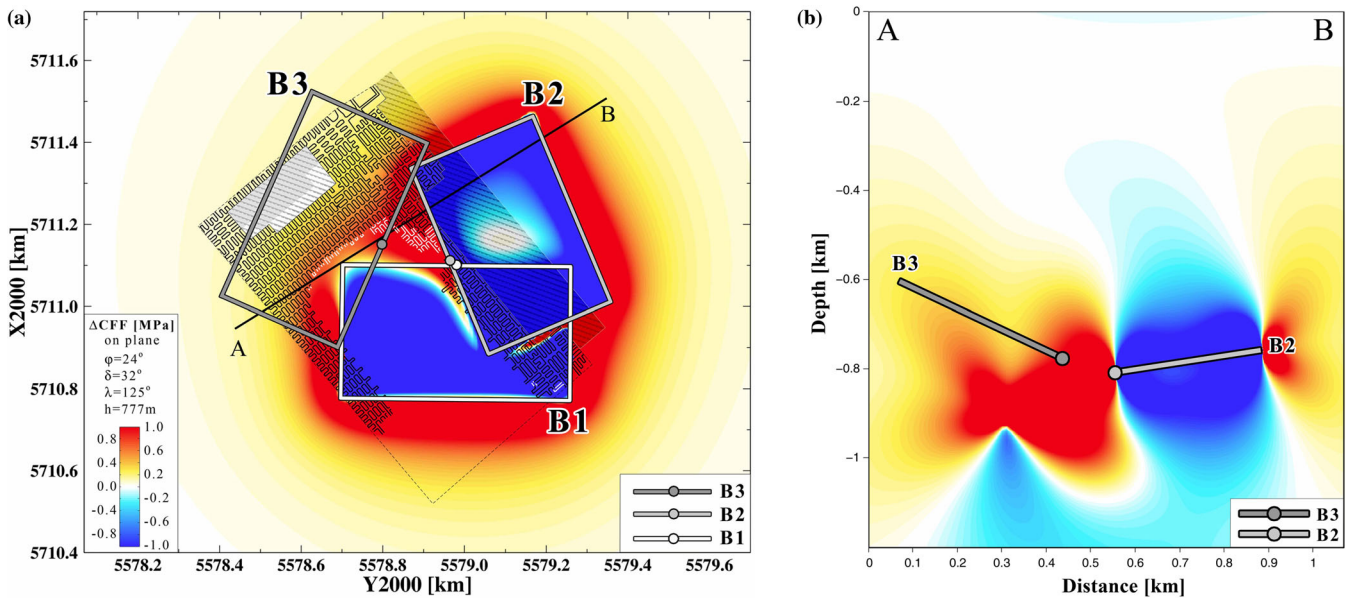


Figure 7. Cumulative Coulomb stress changes due to two events, B1 and B2, calculated on the fault plane of event B3. (a) Horizontal projection. (b) Vertical cross-section along AB profile from (a). The grey dot and grey lines mark, respectively, the rupture starting point and the fault plane boundary of B3 event and white and the light grey dots and white and light grey lines mark these objects of preceding two events, respectively. The cross-hatched area is goaf, the small black rectangles mark a mined-out part and the small white rectangles mark a part being mined from 2010 October 13 to the time of B3 event occurrence.

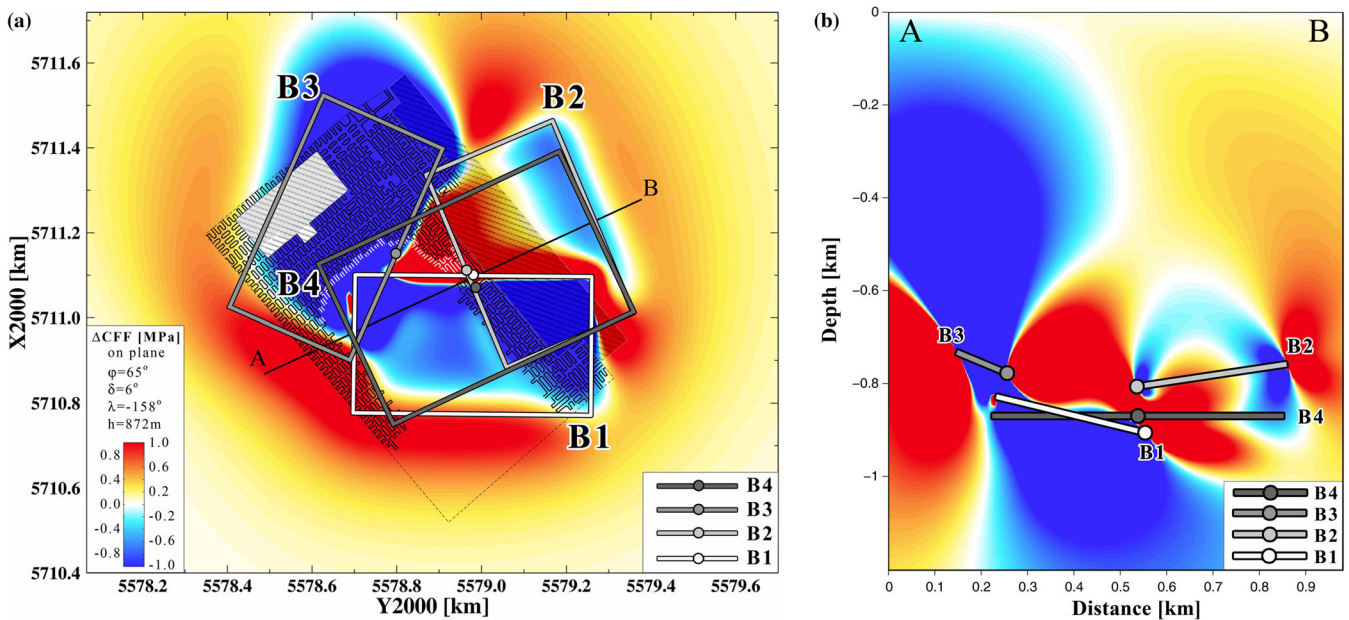


Figure 8. Cumulative Coulomb stress changes due to three events, B1, B2 and B3, calculated on the fault plane of event B4. (a) Horizontal projection. (b) Vertical cross-section along AB profile from (a). The dark grey dot and dark grey lines mark, respectively, the rupture starting point and the fault plane boundary of B4 event and the dots and lines of white and various grey tones mark these objects of preceding three events. The cross-hatched area is goaf, the small black rectangles mark a mined-out part and the small white rectangles mark a part being mined from 2010 December 18 to the time of B4 event occurrence.

B2 event occurred after destressing blasting in the mined out right flank of the panel. Its rupture began above the beginning of B1 event rupture in an area of the stress increase caused by B1 (Fig. 6). B2 exhibited normal faulting, dipping in SWW direction, whereas its rake was directed towards SW. It seems that the oblique faulting of B2 as well as the tensional component in its mechanism was induced by the slip of B1 and the geometrical arrangement of B1 and B2. This physically plausible faulting sequence can also explain why B2 slipping was towards an unmined part.

B3 is an oblique fault dipping towards SEE and slipping close to EW direction. The rupture started in overlapped areas of the increased mining stress and the positive stress change caused by coseismic slips of two preceding events. Also in this case a compressional regime built by the slip of B2 event and mutual arrangement of B2 and B3 rupture planes explain B3 rupture mechanism (Fig. 7). Its EW slip seems to be forced by the tension exerted by the hanging wall of the extensional B2 faulting.

The epicentre of event B4 located close to and ahead of the mining front, in the area where mining stress is high. The event

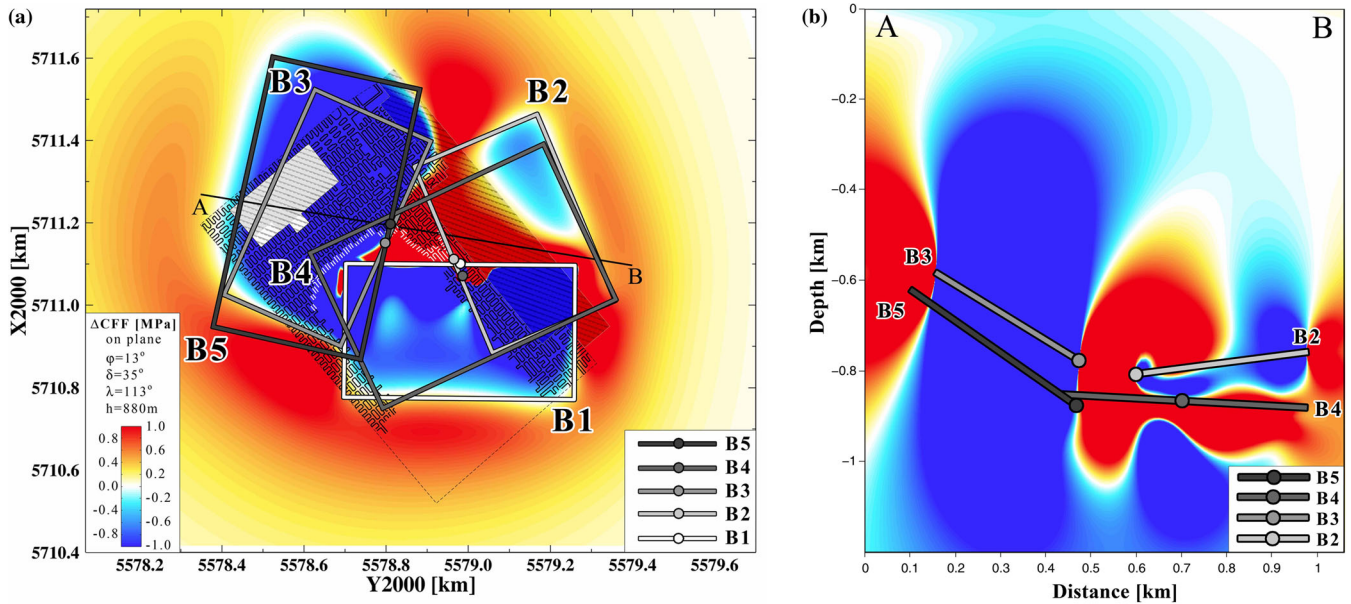


Figure 9. Cumulative Coulomb stress changes due to four events, B1–B4, calculated on the fault plane of event B5. (a) Horizontal projection. (b) Vertical cross-section along AB profile from (a). The black dot and black lines mark, respectively the rupture starting point and the fault plane boundary of B5 event and the dots and lines of white and various grey tones mark the objects of preceding four events. The cross-hatched area is goaf, the small black rectangles mark a mined-out part and the small white rectangles mark a part being mined from 2010 December 18 to the occurrence time of event pair B4, B5.

occurred after destressing blasting from various directions. Could these location and blasting geometry be responsible for the non-directional source of this event? Nevertheless, the location of the B4 rupture starting point between edges of B1 and B2 fault planes and in the area of increased static stress resulted from the three preceding events, suggest that B4 continued fracturing of this rockmass part, which had begun with B1 and B2 events (Fig. 8). This suggestion is also supported by the fact that the directions of B2 and B4 slips are the same. Since B1 occurred more than half a year before B4 and mining in this area could modify significantly the stress transferred from B1 it can be surmised that impact of B2 on B4 was greater than that of B1.

The next event, B5, occurred 1 minute after B4 event. Its rupture began at the edge of the rupture plane of B4 in the area between the positive and negative stress changes caused by all four previous events (Fig. 9). These location and timing apparently indicate correlation between B4 and B5; B5 rupture was a continuation of B4 rupture (Fig. 9b). Furthermore, regarding mutual geometrical setup and, in particular, fault planes orientation and slip directions, the sequence B4–B5 repeated the dynamics of B2–B3 sequence. The compressional regime built by normal faulting towards SW of nearly strike-slipping B4 and enhanced by remnants of the stress transferred from normal faulting of B2 of the same slip direction pushed the B5 hanging wall upwards and in nearly EW direction. A close similarity of B3 and B5 in all aspects: location, orientation, slip, percentage of non-DC components, slope as well as ground effects is striking. It is also worth noting that rupture of B5 continued up to the next static stress enhanced area (Fig. 9b).

Normal faulting of event B4 towards SW seems to be also the causative mechanism for thrust faulting towards S of event B6. B6 similarly as B1 dips north, in agreement with the rock strata inclination direction. The epicentre is located more than 200 m ahead of the mining front towards the unmined part of panel XX/1 (Fig. 10b). The rupture began at the depth of about 890 m at the contact zone of the dolomite and anhydrite layers. Fracturing propagated upwards towards south, opposite to slip, which was 9° from N.

8 SUMMARY AND CONCLUSIONS

In this study six strong tremors from panel XX/1 of Rudna mine have been investigated regarding the untypical ground effects, the complexity of source mechanisms and their interactions. The analysis has indicated the following:

- (1) The events split into three pairs of similar ground effects. The effects of the first pair exceed considerably GMPE estimates at most of observation points, the effects of the second pair are unexpectedly high at short epicentral distances, whereas the effects of the third pair are much less than GMPE estimates at most of observation points.
- (2) All six events demonstrate dominating share of non-DC components in the overall mechanisms and extended rather than point sources.
- (3) Five events have distinct directivity effects. Ruptures occurred along sub-horizontal faults in the direction opposite to dip. The events from the same pairs have similar size and directivity estimates.
- (4) Static stress transfer analysis has signified interrelations between the studied events. The rupture of all events started in the area where Coulomb failure function increased due to the cumulative effect of previous events or at the margin between positive and negative changes of Coulomb stress where their gradient is high. This is especially visible in the case of two last events. Event B5 occurred just after the preceding event, B4. For the last event, B6, stress transfer can justify its, unexplained by mining stresses location (Kozłowska 2013).
- (5) The untypical and diverse ground effects of the studied events result likely from the events' complexity expressed by tensile source mechanisms, finite sources, directivity of ruptures and nearly horizontal rupture planes. The above features seem to be implied by a superposition of coseismic alterations of stress field and stress changes due to mining.
- (6) In particular, the fit of surface maximal amplitude is significantly improved when finite sources are considered instead of point

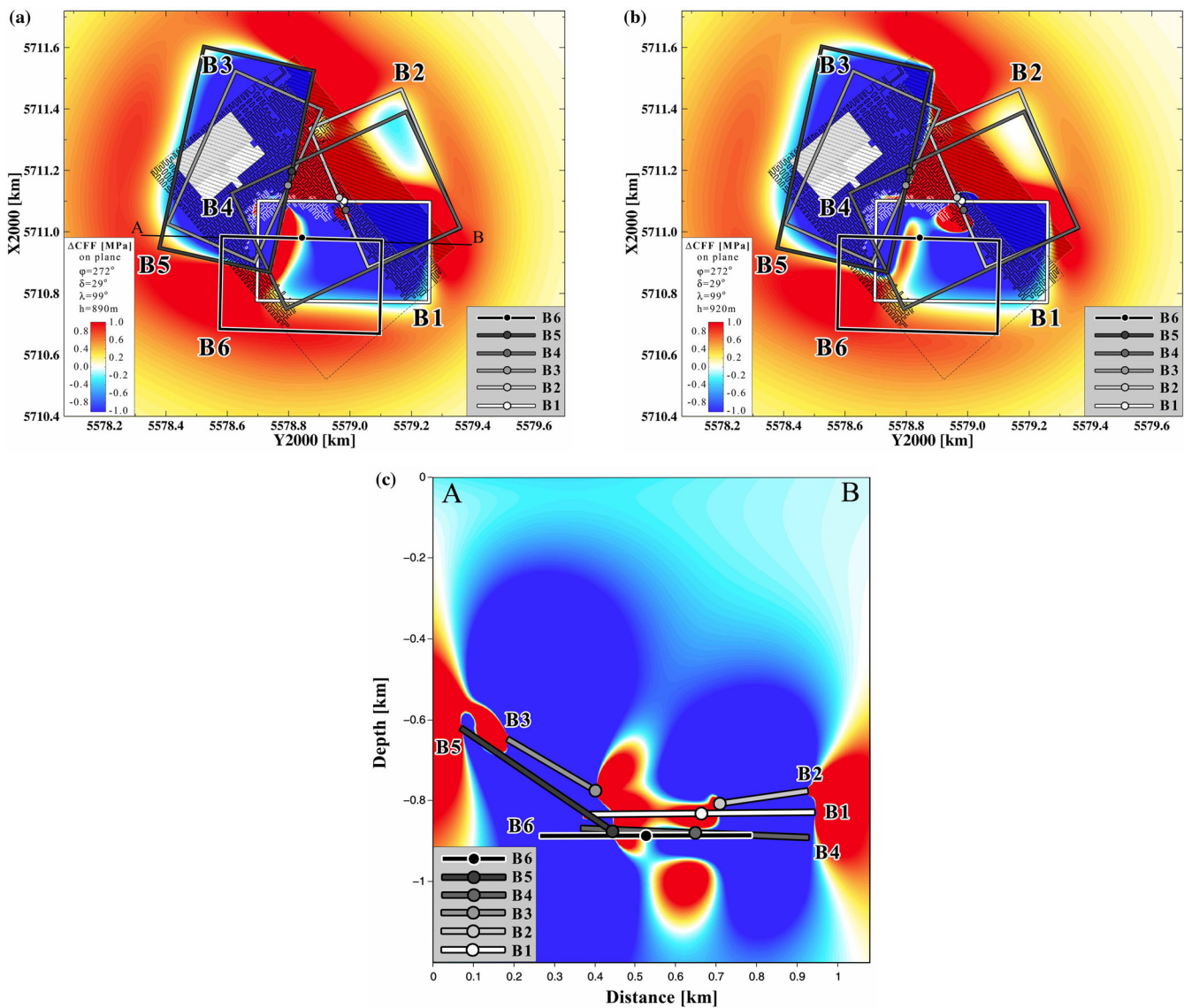


Figure 10. Cumulative Coulomb stress changes due to five events, B1–B5, calculated on the fault plane of event B6. (a) Horizontal projection for B6 located at the depth of 890 m. (b) Horizontal projection for B6 located 30 m below the estimated hypocentral depth, at the depth of 920 m. (c) Vertical cross-section along AB profile from (a). The black dot and black lines with white frames mark, respectively, the rupture starting point and the fault plane boundary of B6 event and the dots and lines of black, white and various grey tones mark these objects of preceding five events. The cross-hatched area is goaf, the small black rectangles mark a mined-out part and the small white rectangles mark a part being mined from 2011 January 20 to the time of B6 event occurrence.

sources. It resulted that the geometry of the surface and directivity effects are more important in order to reproduce the amplitude patterns, than the single radiation pattern of the point sources distributed along these surfaces.

(7) Detailed studies of rupture mechanisms combined with static stress transfer analysis can provide insight into geodynamics of mining seismicity.

(8) Although the local GMPE-s have been built on the basis of huge observational material, one cannot exclude the possibility of significant deviations from the expected ground motion amplitudes, due to specific geodynamics in a part of mine. It is, however, also possible that an analysis like that done within this work can allow foreseeing such extreme surface impacts.

(9) Future investigations should include a time-varying mining stress analysis to complement static stress transfer approach and the detailed source studies in an attempt to identify or whenever

possible avoid such seismic process development, which results in underestimated ground motion. Any reliable solution in this regard would be valuable from practical point of view as it would improve time-dependent seismic hazard assessment in mines.

ACKNOWLEDGEMENTS

This work was supported by National Science Centre, Poland under the research project No. NN525393539 and by the project MINE, which is a part of the R&D-Programme GEOTECHNOLOGIEN and funded by the German Ministry of Education and Research (BMBF), Grant of project BMBF03G0737. The authors would like to thank E. Koziarz, Head of the Geophysical Station of Rudna Mine, for all geological, seismological and mining data. We also wish to express our gratitude to the Editor, Dr Eiichi Fukuyama

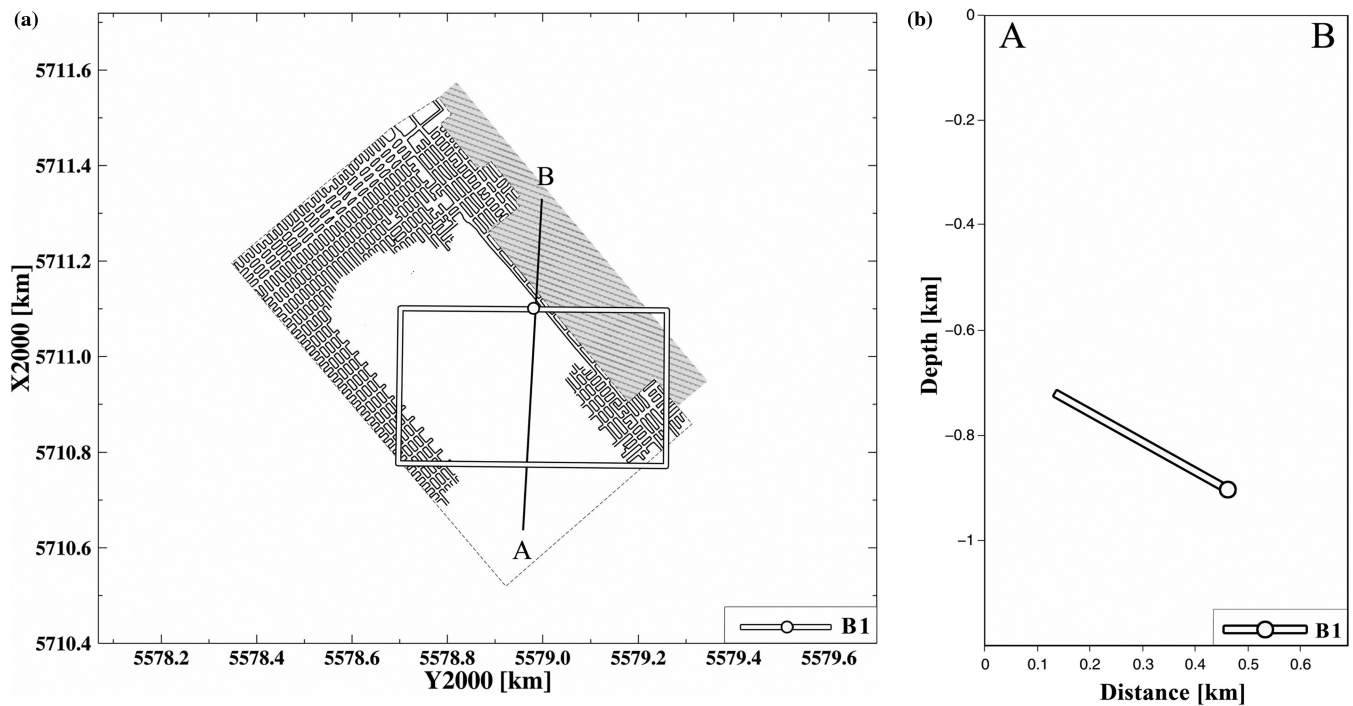


Figure 11. The location of B1 events. (a) Horizontal projection. (b) Vertical cross-section along AB profile from (a). The white dot and white solid lines mark, respectively, the rupture starting point and the fault plane boundary of B1 event. The cross-hatched area is goaf, the small black rectangles mark a mined-out part.

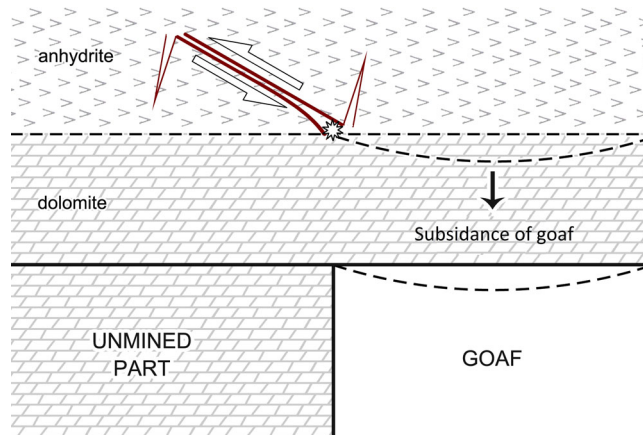


Figure 12. The proposed geomechanical model of the B1 event rupturing. and the anonymous Reviewers for their valuable comments and suggestions.

REFERENCES

- Aki, K. & Richards, P.G., 2002. *Quantitative Seismology*, 2nd edn, University Science Books.
- Andrews, D.J., 1986. Objective determination of source parameters and similarity of earthquakes of different size, in *Earthquake Source Mechanisms*, Maurice Ewing Vol. 6, pp. 259–267, eds Das, S., Boatwright, J. & Scholz, C.H., Am. Geophys. Union.
- Brune, J.N., 1970. Tectonic stress and the spectra seismic shear waves from earthquakes, *J. geophys. Res.*, **75**, 4997–5009.
- Brune, J.N., 1971. Correction, *J. geophys. Res.*, **76**, 5002.
- Cesca, S., Heimann, S., Stammer, K. & Dahm, T., 2010. Automated procedure for point and kinematic source inversion at regional distances, *J. geophys. Res.*, **115**, B06304, doi:10.1029/2009JB006450.

- Cesca, S., Rohr, A. & Dahm, T., 2013. Discrimination of induced seismicity by full moment tensor inversion and decomposition, *J. Seismol.*, **17**, 147–163.
- Cocco, M. & Rice, J.R., 2002. Pore pressure and poroelasticity effects in Coulomb stress analysis of earthquake interactions, *J. geophys. Res.*, **107**, doi:10.1029/2000JB000138.
- Eyre, T.S. *et al.*, 2013. Moment tensor inversion for the source location and mechanism of long period (LP) seismic events from 2009 at Turrialba volcano, Costa Rica, *J. Volc. Geotherm. Res.*, **258**, 215–223.
- Gibowicz, S.J. & Kijko, A., 1994. *An Introduction to Mining Seismology*, Academic Press.
- Golik, A. & Mendecki, M.J., 2012. Ground motion prediction equations for induced seismicity in the Main Anticline and Main Syncline, Upper Silesian Coal Basin, Poland, *Acta Geophys.*, **60**, 410–425.
- Hainzl, S., Enescu, B., Cocco, M., Woessner, J., Catalli, F., Wang, R. & Roth, F., 2009. Aftershock modeling based on uncertain stress calculations, *J. geophys. Res.*, **114**, B05309, doi:10.1029/2008JB006011.
- Haskell, N.A., 1953. The dispersion of surface waves in multilayered media, *Bull. seism. Soc. Am.*, **43**, 17–34.
- Heimann, S., 2011. A robust method to estimate kinematic earthquake source parameters, *PhD thesis*, Univ. Hamburg, Germany.
- King, G.C.P. & Cocco, M., 2001. Fault interaction by elastic stress changes: new clues from earthquake sequences, *Adv. Geophys.*, **44**, 1–38.
- King, G.C.P., Stein, R.S. & Lin, J., 1994. Static stress changes and the triggering of earthquakes, *Bull. seism. Soc. Am.*, **84**, 935–953.
- Knopoff, L. & Randall, M.J., 1970. The compensated linear-vector dipole: a possible mechanism for deep earthquakes, *J. geophys. Res.*, **75**, 4957–4963.
- Kozłowska, M., 2013. Analysis of spatial distribution of mining tremors occurring in Rudna copper mine (Poland), *Acta Geophys.*, **61**, 1156–1169.
- Kwiatak, G., 2011. FOCI—software for calculation of the seismic moment tensor and source parameters in mining environment [online], Available at: <http://www.sejsmologia-gornicza.pl/projekty/foci>.
- Lasocki, S., 2013. Site specific prediction equations for peak ground acceleration of ground motion due to earthquakes induced by underground

- mining in Legnica-Głogów Copper District in Poland, *Acta Geophys.*, **61**, 1130–1155.
- Lasocki, S. & Olszewska, D., 2003. The influence of non-homogeneous local effects on the accuracy of prediction of strong ground motion propagation: an example from the town Polkowice region, in *Natural Hazards in Mining. Proc VIII Mining Workshop*, Wyd. IGSMiE PAN, Kraków, pp. 113–126, ed. Pilecka, E. (in Polish, English Abstract).
- Lin, J. & Stein, R.S., 2004. Stress triggering in thrust and subduction earthquakes, and stress interaction between the southern San Andreas and nearby thrust and strike-slip faults, *J. geophys. Res.*, **109**, B02303, doi:10.1029/2003JB002607.
- Niewiadomski, J., 1997. Spectral analysis and seismic source parameters, in *Seismic Monitoring in Mines*, pp. 144–158, ed. Mendecki, A.J., Chapman & Hall.
- Olszewska, D., 2006. Attenuation relations of ground motion acceleration response spectra for the Polkowice region, *Publ. Inst. Geophys. Pol. Acad. Sci.*, **M-29**(395), 161–174.
- Orlecka-Sikora, B., 2010. The role of static stress transfer in mining induced seismic events occurrence, a case study of the Rudna mine in the Legnica-Głogow Copper District in Poland, *Geophys. J. Int.*, **182**, 1087–1095.
- Orlecka-Sikora, B., Lizurek, G. & Rudziński, Ł., 2011. The Static Stress Transfer in the seismogenic process by example of the Rudna mine, *Polish Mining Rev.*, **67**(6), 76–85 (in Polish, English Abstract).
- Orlecka-Sikora, B., Lasocki, S., Lizurek, G. & Rudziński, Ł., 2012. Response of seismic activity in mines to the stress changes due to mining induced strong seismic events, *Int. J. Rock. Mech. Min. Sci.*, **53**, 151–158.
- Papadimitriou, E.E. & Sykes, L.R., 2001. Evolution of the stress field in the northern Aegean Sea (Greece), *Geophys. J. Int.*, **146**, 747–759.
- Rudziński, Ł. & Dębski, W., 2011. Extending the double-difference location technique to mining applications. Part I: numerical study, *Acta Geophys.*, **59**(4), 785–814.
- Sen, A.T., Cesca, S., Bischoff, M., Meier, T. & Dahm, T., 2013. Automated full moment tensor inversion of coal mining-induced seismicity, *Geophys. J. Int.*, **195**(2), 1267–1281.
- Stein, R.S., 1999. The role of stress transfer in earthquake occurrence, *Nature*, **402**(6762), 605–609.
- Toda, S., Stein, R.S., Richards-Dinger, K. & Bozkurt, S.B., 2005. Forecasting the evolution of seismicity in southern California: animations built on earthquake stress transfer, *J. geophys. Res.*, **110**, B05S16, doi:10.1029/2004JB003415.
- Vavryčuk, V., 2001. Inversion for parameters of tensile earthquakes, *J. geophys. Res.*, **106**, 16 339–16 355.
- Vavryčuk, V., 2011. Tensile earthquakes: theory, modeling, and inversion, *J. geophys. Res.*, **116**, B12320, doi:10.1029/2011JB008770.
- Wiejacz, P., 1991. Investigation of focal mechanisms of mine tremors by the moment tensor inversion, *PhD thesis*, Inst. Geophys. Pol. Ac. Sci., Warsaw, Poland.
- Wiejacz, P., 1992. Calculation of seismic moment tensor for mine tremors from the Legnica-Głogów Copper Basin, *Acta geophys. Pol.*, **40**, 103–122.
- Wyss, M. & Brune, J.N., 1968. Seismic moment, stress and source dimensions for earthquakes in the California-Nevada region, *J. geophys. Res.*, **73**, 4681–4694.